



Peripheral positions encode transport specificity in the small multidrug resistance exporters

Olive E. Burataª, Ever O'Donnellº 🗓, Jeonghoon Hyunʰ, Rachael M. Luceroª, Junius E. Thomasª 🗓, Ethan M. Gibbsʰ 🗓, Isabella Reacherʰ, Nolan A. Carneyª, and Randy B. Stockbridge^{a,b,1}

Edited by Dirk-Jan Slotboom, Rijksuniversiteit Groningen, Groningen, Netherlands; received February 19, 2024; accepted May 2, 2024 by Editorial Board Member Nieng Yan

In secondary active transporters, a relatively limited set of protein folds have evolved diverse solute transport functions. Because of the conformational changes inherent to transport, altering substrate specificity typically involves remodeling the entire structural landscape, limiting our understanding of how novel substrate specificities evolve. In the current work, we examine a structurally minimalist family of model transport proteins, the small multidrug resistance (SMR) transporters, to understand the molecular basis for the emergence of a novel substrate specificity. We engineer a selective SMR protein to promiscuously export quaternary ammonium antiseptics, similar to the activity of a clade of multidrug exporters in this family. Using combinatorial mutagenesis and deep sequencing, we identify the necessary and sufficient molecular determinants of this engineered activity. Using X-ray crystallography, solid-supported membrane electrophysiology, binding assays, and a proteoliposome-based quaternary ammonium antiseptic transport assay that we developed, we dissect the mechanistic contributions of these residues to substrate polyspecificity. We find that substrate preference changes not through modification of the residues that directly interact with the substrate but through mutations peripheral to the binding pocket. Our work provides molecular insight into substrate promiscuity among the SMRs and can be applied to understand multidrug export and the evolution of novel transport functions more generally.

multidrug exporter | transporter | EmrE | substrate specificity | antiseptic

The constraints of the two-dimensional membrane environment limit the number of folds available to membrane proteins (1). And yet, through evolution, a relatively small number of conserved folds have radiated into functionally diverse transporters that are able to translocate all of the structurally and chemically diverse solutes necessary for life (2). Because large conformational changes are inherent to transporter function, this functional divergence requires alterations to substrate binding in the ground state, as well as the entire structural and energetic landscape during the conformational change. Understanding the molecular basis of how novel transport functions emerge through evolution is thus a challenging question.

We have established proteins from the small multidrug resistance (SMR) family as a tractable system to analyze how changes in substrate specificity arise through molecular events. These proteins are among the smallest characterized membrane transport proteins, with only ~one hundred residues in total. Pairs of identical subunits assemble as antiparallel homodimers (3). This assembly gives rise to a symmetric energy landscape with structurally and energetically equivalent inward- and outward-facing structures (4). This primitive architecture was a likely evolutionary antecedent to the pseudosymmetric inverted repeat architecture that is common among secondary active transporters (5). Thus, the SMRs provide a general model for the early evolution of transport proteins (6).

SMR transporters are widespread among microorganisms and have evolved several distinct functional subtypes (7). Two of these are considered in this article: the SMR_{Gdx} (guanidinium export) and the SMR_{Qac} (quaternary ammonium cation). The SMR_{Gdx} selectively transports guanidinium ion (Gdm⁺), a small cationic by-product of nitrogen metabolism (8), along with close polar analogs like guanylurea (9, 10). In contrast, transporters from the SMR_{Oac} subtype are promiscuous exporters of hydrophobic cationic compounds (11-13), including quaternary ammonium compounds like benzalkonium and cetyltrimethylammonium (also known as cetrimonium or CTA⁺), the main antiseptic agents in common household and hospital cleaning solutions and antibacterial handsoaps (14). Genes encoding SMR_{Qac} transporters are among the most frequent genes associated with horizontal transfer of drug resistance among bacterial populations (15-17). The SMR_{Oac} subtype includes the well-studied multidrug exporter from *Escherichia coli*, EmrE.

Significance

Drug exporters from the small multidrug resistance (SMR) family protect bacteria against structurally diverse quaternary ammonium antiseptics, including common agents found in antibacterial handsoaps and antiseptic cleaning solutions. The molecular basis for their promiscuous transport activity remains an open question. By engineering a closely related, but very selective protein from the same family to transport structurally distinct antiseptics, we show that residues peripheral to the substrate binding site are necessary and sufficient for promiscuous transport. These results show that key determinants of substrate transport specificity extend beyond the direct substate/ binding site interactions and provide insight into how multidrug exporters might have evolved.

Author affiliations: ^aProgram in Chemical Biology, University of Michigan, Ann Arbor, MI 48109; and ^bDepartment of Molecular, Cellular, and Developmental Biology, University of Michigan, Ann Arbor, MI 48109

Author contributions: O.E.B., E.O., R.M.L., J.E.T., N.A.C., and R.B.S. designed research; O.E.B., E.O., J.H., R.M.L., E.M.G., I.R., and R.B.S. performed research; O.E.B., J.E.T., and N.A.C. contributed new reagents/analytic tools; O.E.B., E.O., J.H., R.M.L., E.M.G., I.R., N.A.C., and R.B.S. analyzed data; and O.E.B. and R.B.S. wrote the paper.

The authors declare no competing interest.

This article is a PNAS Direct Submission. D.-J.S. is a guest editor invited by the Editorial Board.

Copyright © 2024 the Author(s). Published by PNAS. This article is distributed under Creative Commons Attribution-NonCommercial-NoDerivatives License 4.0 (CC BY-NC-ND).

¹To whom correspondence may be addressed. Email: stockbr@umich.edu.

This article contains supporting information online at https://www.pnas.org/lookup/suppl/doi:10.1073/pnas. 2403273121/-/DCSupplemental.

Published June 12, 2024

Despite their substantial differences in substrate transport specificity, transporters from the SMR $_{\rm Gdx}$ and SMR $_{\rm Qac}$ subtypes exhibit high structural (1.2 Å C_{α} rmsd) and sequence (~40%) similarity (7, 18). The proteins share an absolutely conserved pair of central glutamates at the bottom of the substrate binding pocket, which bind the cationic substrate or protons in a mutually exclusive fashion (19). In fact, most of the residues that line the substrate binding pocket are conserved (18), raising the question of how these substantial changes in substrate selectivity arose without altering the protein residues in closest proximity to the substrate.

Comparative structural studies of EmrE and the best-studied SMR_{Gdx}, from *Clostridales* oral taxon 876, called Gdx-Clo, revealed key differences in the interactions between these conserved residues (10, 18). Whereas the binding pocket sidechains in Gdx-Clo are organized in a polarized hydrogen bond network that stabilizes the substrate- and proton-binding central glutamates, in EmrE, a weak and disorganized hydrogen bond network yields more rotameric freedom for binding pocket sidechains (18). EmrE structures solved in complex with substrates of varying bulk and aromatic character show that this flexibility—especially of the central glutamates (E13) and binding site aromatic W63—accommodates structurally dissimilar substrates (18). Despite these recent structural advances, the molecular determinants of promiscuous substrate transport in EmrE remain unknown. Numerous mutant proteins have been examined, and perturbations to transport selectivity have been described for many of them (20–22). At the same time, a series of biophysical experiments have established detailed information about EmrE's dynamic properties (4, 23-27), which have been invoked to explain transport promiscuity. However, these studies have not coalesced into a unified understanding of the specific protein sequences that underlie the emergence of promiscuous transport behavior characteristic of the SMR_{Oacs} within the larger SMR family.

In order to understand the molecular features responsible for substrate polyspecificity among SMRs, we engineer Gdx-Clo to transport structurally dissimilar quaternary ammonium antiseptics. Using combinatorial mutagenesis, we establish a set of residues that are necessary and sufficient for this activity. These residues are conserved among SMR $_{\rm Qacs}$, supporting the interpretation that these residues also reflect natural mutations that led to promiscuous transport by the SMR $_{\rm Qacs}$. By combining structural studies, binding, transport, and electrophysiology assays, we establish the mechanistic basis for quaternary ammonium antiseptic transport by this family of transporters.

Results

An Engineered Variant of Gdx-Clo Confers Resistance to Quaternary Ammonium Antiseptics. Analysis of sequence alignments of the ${\rm SMR_{Qac}}$ and ${\rm SMR_{Gdx}}$ transporters (7) revealed six residues that are highly conserved in each subtype, but that differ between the subtypes. These residues were, for Gdx-Clo and EmrE, respectively, Gly10/Ile11, Trp16/Gly17, Ala17/Thr18, Met39/Tyr40, Ala67/Ile68, and Lys101/Asn102. We reasoned that these residues might be mainly responsible for the differing substrate selectivity of the SMR_Qac and SMR_Gdx subtypes. We therefore introduced the SMR_Qac residues at all six positions in Gdx-Clo (G10I, W16G, A17T, M39Y, A67I, and K101N), but the resulting transporter failed to confer bacterial resistance to quaternary ammonium antiseptics (SI Appendix, Fig. S1).

To identify additional mutations that might furnish quaternary ammonium resistance and substrate polyselectivity, we further subjected this mutated Gdx-Clo construct to random mutagenesis followed by selection for bacterial growth in the presence of

cetrimonium (CTA+). Surviving variants were further tested for survival in tetrapropylammonium (TPA+) to select for promiscuous transporters. We chose these substrates because they differ in the bulkiness of the quaternary ammonium group, and cetrimonium (but not TPA+) possesses a long alkyl tail characteristic of many common quaternary ammonium antiseptics. Moreover, the differing inhibitory concentrations of these two compounds (~200 μM and ~20 mM, respectively) demand export efficiency over ~2 orders of magnitude concentration. Using this selection protocol, one round of directed evolution yielded a construct that supported robust growth of $\Delta emrEE$. coli in the presence of both CTA⁺ and TPA+. This construct bore the six original rationally designed mutations and an additional seventh mutation, A60T. The resistance conferred by this construct, dubbed Gdx-Clo-7x, is comparable to that of native EmrE introduced on a rescue plasmid (Fig. 1A). By themselves, none of the seven mutants, including A60T, exhibit appreciable quaternary ammonium resistance (SI Appendix, Fig. S3). Four of the single-mutant variants (G10I, W16G, M39Y, and A67I) fail to confer any resistance at all. The remaining three (A17T, A60T, and K101N) exhibit marginal resistance, with some growth observed at the lowest culture dilutions, corresponding to ~1,000-fold diminished resistance relative to Gdx-Clo-7x.

The seven mutations of Gdx-Clo-7x are distributed across the protein in three structurally colocalized clusters (Fig. 1B). The first, G10I (red), occurs at a helical packing motif between helices 1 and 3 (Fig. 1 C, Left). These helices contribute several residues to the binding site hydrogen bond network, suggesting that the G10I mutation alters the packing of these two helices and disrupts hydrogen bond interactions among substrate binding site sidechains. We previously proposed that disruption of the hydrogen bond network in the binding site permits binding of structurally diverse substrates (18). The second mutant cluster is composed of W16G, A17T, and M39Y (orange), located adjacent to the substrate binding site (Fig. 1 C, Center). W16 is the only one of the seven mutant residues that participates in the hydrogen bond network of WT Gdx-Clo's substrate binding site, where it directly coordinates the central glutamate, E13. In WT Gdx-Clo, hydrophobic sidechains A17 and M39 sandwich W16 in place. A60T, A67I, and K101N (green) comprise the third cluster, which is located at the periphery of the aqueous binding pocket (Fig. 1 C, Right). These residues undergo large changes in position during the inward- to outward-facing conformational change, and interpolation of the inward- and outward-facing structures suggests that they might pass in close proximity during the conformational transition.

Gdx-Clo-7x Binds and Transports Quaternary Ammonium Substrates, but Not Gdm⁺. We next examined the functional and biochemical properties of Gdx-Clo-7x. Size exclusion chromatography showed a monodisperse peak with protein yield comparable to WT Gdx-Clo (SI Appendix, Fig. S4). We first assessed substrate binding by monitoring substrate-dependent changes to the proteins' intrinsic tryptophan fluorescence (9, 28) (Fig. 2 A-C). The seven mutations induce a complete switch in substrate preference for Gdm⁺ and TPA⁺: Gdx-Clo WT binds Gdm⁺ with a K_d of 800 µM, with no characteristic fluorescence increase upon titration with TPA⁺. In contrast, Gdx-Clo-7x binds TPA⁺ with a K_d of 15 mM, in line with the inhibitory concentration used for the bacterial selection experiments, but not Gdm⁺ (K_d >50 mM). Both WT and mutant transporter bind CTA+ with comparable affinities (7.2 μM for WT Gdx-Clo and 4.7 μM for Gdx-Clo-7x), in agreement with previous data showing detergent binding by members of the SMR_{Gdx} subtype (29). Together, these binding experiments confirm Gdx-Clo-7x's interaction with both

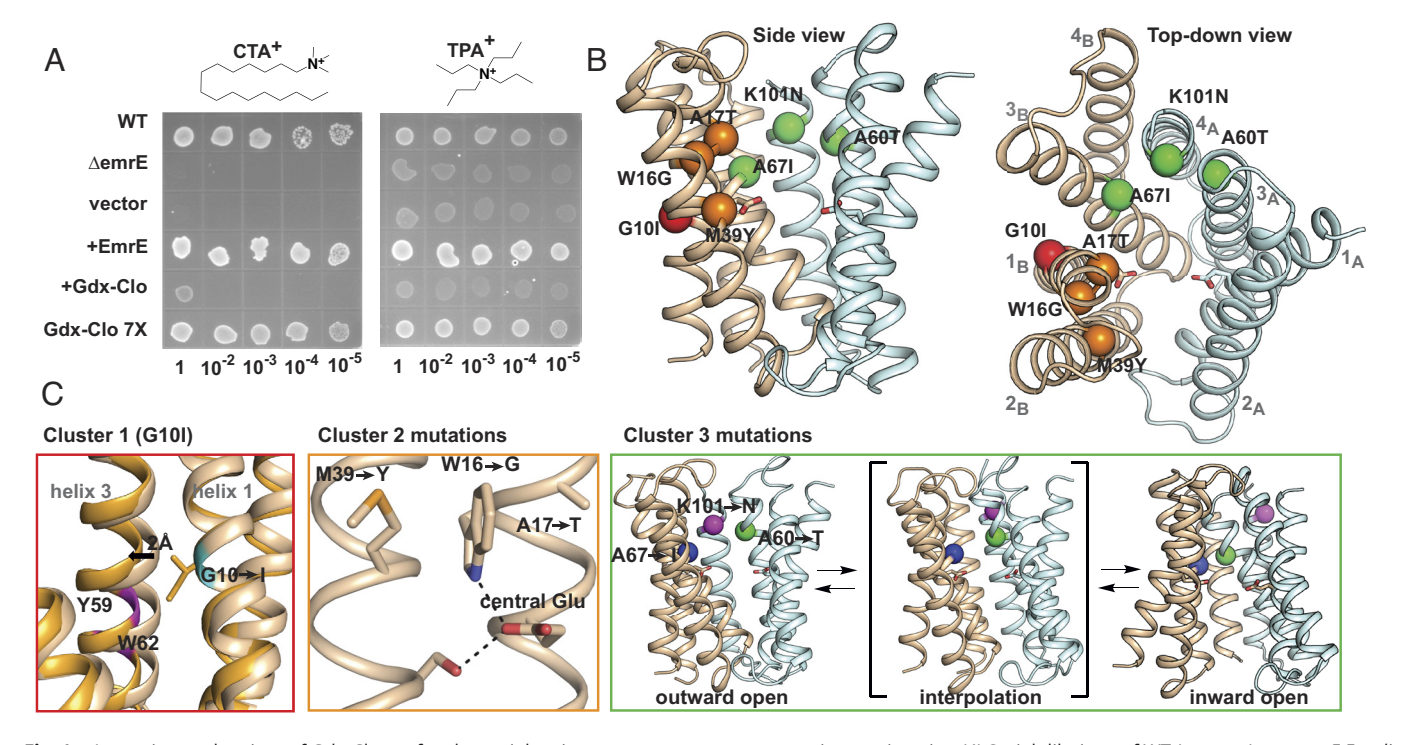


Fig. 1. An engineered variant of Gdx-Clo confers bacterial resistance to quaternary ammonium antiseptics. (A) Serial dilutions of WT (top row) or ΔemrE E. coli (bottom 5 rows) bearing plasmids with SMR variants as indicated. Selections were performed with 120 µM CTA⁺ (Left) or 18 mM TPA⁺ (Right). Control dilutions on no-drug control plates are shown in SI Appendix, Fig. S2. (B) Structure of WT Gdx-Clo (PDB: 6WK8) with Ca atoms of the Gdx-Clo-7x mutations shown as spheres. The A and B monomers are shown in pale cyan and tan, respectively, and the central glutamates are shown as sticks. Transmembrane helices are numbered in gray text. For clarity, mutations are shown on only one monomer. Mutations are colored according to structurally colocalized cluster, as described in the text (cluster 1: red; cluster 2: orange; cluster 3: green). (C) Left, overlay of the B monomer of Gdx-Clo (tan; PDB:6WK8) and EmrE (orange; PDB: 7MH6) with the position of cluster 1 mutation (G10/I11) shown in cyan. The positions of binding site residues Y59 and W62 (Gdx-Clo numbering) are shown in magenta. Middle: WT Gdx-Clo with positions of cluster 2 mutations, the central glutamate, and S42 shown as sticks. Hydrogen bond interactions are shown as dashed lines. Right: Interpolation of outward- and inward-facing Gdx-Clo with C_w atoms of cluster 3 mutations shown as spheres (A67 in blue, K101 in magenta, and A60 in green).

quaternary ammonium substrates and show that the expanded recognition of quaternary ammonium compounds is accompanied by greatly diminished binding to Gdm⁺.

We sought to examine the structural basis for quaternary ammonium binding, but we were unable to produce crystals that diffracted to high resolution for Gdx-Clo-7x, or for WT Gdx-Clo in the presence of CTA⁺. We screened some of the single-mutant constructs for crystallization and diffraction and obtained serviceable crystals for Gdx-Clo A60T that allowed us to determine its structure in complex with CTA+ (SI Appendix, Table S1). The

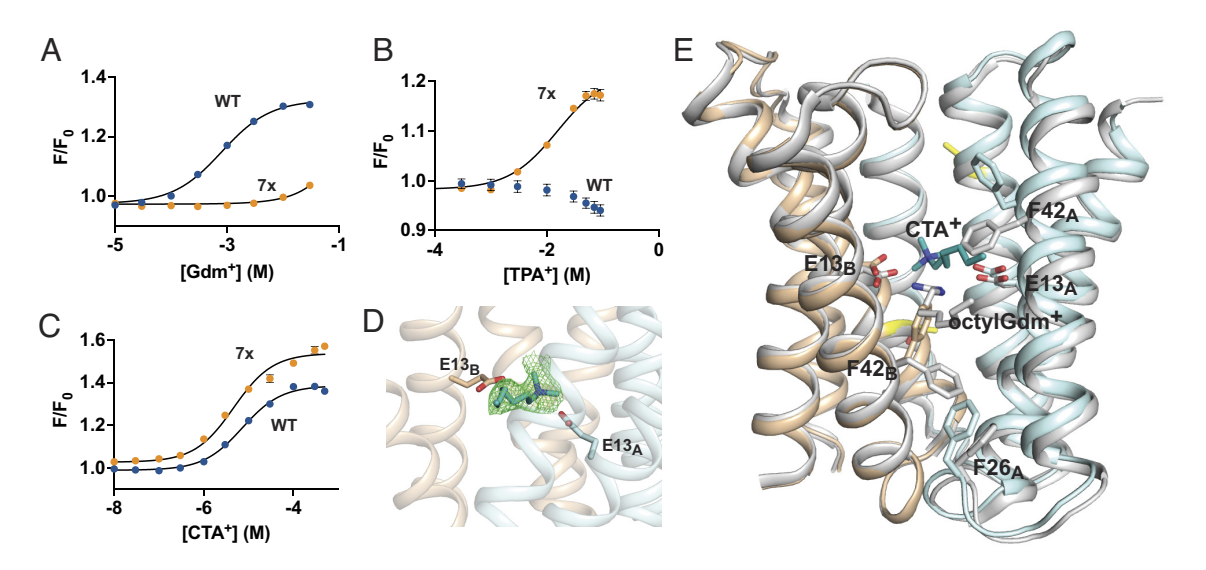


Fig. 2. Substrate binding to WT Gdx-Clo and Gdx-Clo-7x. Tryptophan fluorescence as a function of (A) Gdm⁺, (B) TPA⁺, or (C) CTA⁺ concentration, normalized relative to fluorescence intensity in the absence of substrate, for WT Gdx-Clo (blue) and Gdx-Clo-7x (orange). Each datapoint represents the mean and SEM of three individual titrations (where not visible, error bars are smaller than the diameter of the point). Solid lines represent fits to a single-site binding model. K_d values derived from these fits are reported in the text. Raw fluorescence spectra are shown in SI Appendix, Fig. S5. Data from an independent protein preparation are shown in SI Appendix, Fig. S6. (D) Structure of CTA+ bound to Gdx-Clo A60T. A and B subunits are shown in pale cyan and tan, respectively, and the central glutamates are shown as sticks. Modeled atoms of CTA⁺ are shown in teal, with the F_0 - F_c polder omit map, contoured at 4σ , in green. (E) Overlay of Gdx-Clo A60T with CTA⁺ bound (colored as in panel D) and WT Gdx-Clo with octylGdm⁺ bound (PDB:6WK9; shown in light gray). The A60T residues are colored in yellow.

overall structure was nearly identical to WT Gdx-Clo (C_{α} rmsd = 0.24 Å), and the positions and interactions among major binding site residues (E13, W16, Y59, W62) are unchanged relative to WT Gdx-Clo. We observe only minor perturbations to the structure in the vicinity of the A60T residues, which are located ~10 Å from, and face away from, the binding site. Moreover, functional experiments show that A60T transports Gdm⁺ at levels similar to WT Gdx-Clo (SI Appendix, Fig. S7). We therefore interpret this structure to provide insight into how WT Gdx-Clo binds CTA⁺ (Fig. 2*C*). We observed an elongated density in the binding pocket, into which we modeled the quaternary ammonium headgroup and the first seven carbons of the alkyl tail of CTA+ (Fig. 2D). The quaternary ammonium headgroup is located in the vicinity of the central glutamates, but binds about 2.5 Å higher, and about 4 Å farther back in the pocket than do the transported guanidinyl substrates, which reside in the same plane as the glutamates (10) (Fig. 2E). The alkyl tail of CTA⁺ extends toward the membrane, exiting the binding site through a gap between helices 2_A and 2_B, in the manner observed for the extended alkyl tail of octylGdm⁺ (10). Due to the slightly higher position of the substrate within the binding pocket, the hydrophobic residues that line the membrane portal, notably F42_A and F42_B, rearrange to permit the tail to access the membrane (Fig. 2E). This structure suggests that although some quaternary ammoniums with small headgroups can be accommodated within the WT binding pocket, these substrates are unable to access its deepest point between the central glutamates, which could plausibly impair their ability to induce conformational change of the transporter.

We further assessed transport of TPA⁺ by Gdx-Clo-7x using solid-supported membrane (SSM) electrophysiology (Fig. 3A). Due to its hydrophobicity, TPA+ elicits sizeable positive currents that reflect protein-independent interactions between the cationic substrate and the membrane (SI Appendix, Fig. S8). However, for Gdx-Clo-7x, titration with mM concentrations of TPA+ also yields small negative capacitive currents that evolve more slowly than the TPA⁺ binding currents. These currents are consistent with electrogenic proton/TPA+ antiport. Peak current amplitudes, which reflect the initial rate of transport, were well fit by the Michaelis-Menten equation with a K_m value of 6.2 mM (Fig. 3B). For comparison, EmrE transports TPA+ with a K_m value of 800 μM (18). Gdm^+ currents were nearly undetectable for the Gdx-Clo-7x mutant, but, as in EmrE, increasingly hydrophobic substitutions of the guanidinium moiety restored transport (Fig. 3C). This trend differs from WT Gdx-Clo, for which hydrophobic substitution diminishes a substrate's initial rate of transport (10).

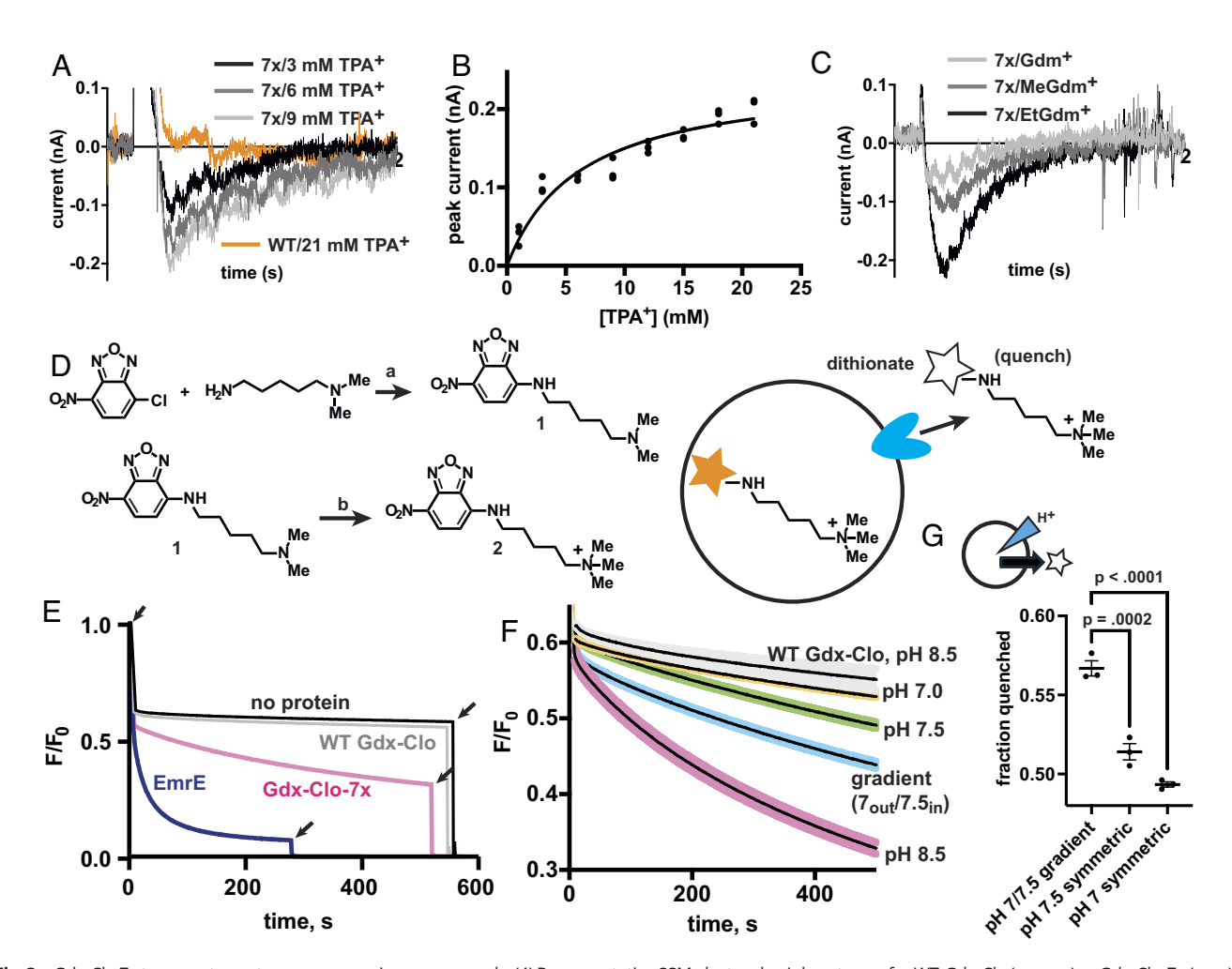
We were unable to assess CTA+ transport using SSM electrophysiology, due to CTA+'s detergent-like properties that cause it to partition into the membrane. To develop an assay for this antiseptic, we leveraged our structural observation that CTA+ binds with its alkyl tail extending out through a lateral portal in the protein and into the membrane, shown in Fig. 2. This allowed us to adapt an approach used to study lipid transport by lipid transport proteins (30-32), which bind substrate lipids in a similar manner (33). We chemically synthesized a novel substrate analog with a fluorophore, nitrobenzoxadiazole (NBD), conjugated to an aliphatic 5-carbon linker with a trimethylammonium headgroup (NBD-TA+, Fig. 3D). Based on our structure, if the quaternary ammonium headgroup binds similarly in the binding pocket, we expect the hydrophobic linker and NBD to extend through the portal and into the membrane, similar to the interaction between scramblases and NBD-conjugated lipids. For the assay, NBD-TA⁺ is incorporated into proteoliposomes. The addition of dithionate to the external buffer quenches the fluorescence

of external NBD-TA⁺, including NBD-TA⁺ in the outer membrane leaflet, reducing the signal by about half. For proteoliposomes reconstituted with EmrE (~2 to 3 transporters per liposome), fluorescence continues to decrease by 80% over ~200 s, reflecting protein-mediated export or exchange of NBD-TA⁺. Addition of triton at the end of the experiment solubilizes the lipid vesicles, permitting complete quenching of the remaining protected NBD (Fig. 3E). Control experiments showed that NBD by itself is not transported. In contrast, for protein-free liposomes, the fluorescence signal from internal NBD-TA⁺ remains steady after the initial quenching step. Likewise, as anticipated from the resistance assays, minimal NBD-TA⁺ transport is observed for WT Gdx-Clo proteoliposomes.

We next sought to evaluate NBD-TA⁺ transport by Gdx-Clo-7x. Independent quantitative western blots of proteoliposomes show that Gdx-Clo-7x is not incorporated into proteoliposomes as efficiently as WT Gdx-Clo (P = 0.046; SI Appendix, Fig. S9 and Table S2). By increasing the protein input for the reconstitution, we were able to prepare Gdx-Clo-7x liposomes that contained a comparable amount of protein relative to the WT Gdx-Clo proteoliposomes (P = 0.55). Under these conditions, we observed clear transport of NBD-TA⁺ by Gdx-Clo-7x that is pH-dependent with near-maximal activity at pH 8.5 (Fig. 3E and SI Appendix, Fig. S11). For comparison, the pH optimum for substrate exchange by EmrE is ~8.0 (34). Transport catalyzed by Gdx-Co-7x plateaued at a higher F/F₀ value than for EmrE, which likely indicates that some of the reconstituted Gdx-Clo-7x is inactive. Based on the approximate half-times of the transport reaction (~250 s. for the Gdx-Clo-7x sample and ~12 s. for the EmrE sample) and estimates of the liposome occupancy—two to three copies of EmrE per liposome and at most one copy of Gdx-Clo per liposome, derived from the F/F₀ plateau according to Poisson statistics (35)—we estimate that the rate of NBD-TA+ transport by Gdx-Clo-7x is about fivefold to 10-fold slower than EmrE. When an inward-directed pH gradient is imposed, substrate export and, as a result, quenching is significantly accelerated, as anticipated for a proton-coupled antiporter (Fig. 3 F and G). Together, the TPA+ and NBD-TA+ transport assays link the resistance phenotype to active, proton-coupled transport of both quaternary ammonium substrates.

The Majority of Mutations Are Essential for Quaternary Ammonium Resistance. To assess whether all seven mutations introduced in Gdx-Clo-7x are essential for quaternary ammonium transport and resistance activity, or whether a subset of these mutations would be sufficient for this activity, we developed a modified Gibson assembly method to construct a combinatorial library of all 128 possible variants of the seven mutations (Fig. 4A). This library was transformed into $\Delta emrE\ E.\ coli$ cells (at a ratio that ensured that each bacterial cell possessed only one plasmid) and plated, with or without antiseptic selection. The pooled plasmid DNA isolated from the resulting colonies was then analyzed using next-generation sequencing (NGS; SI Appendix, Table S3). We elected to plate the bacteria to isolate any colonies with appreciable growth, rather than perform a competitive growth in liquid culture so that any potential variant with low fitness would not be outcompeted during the growth. For each selection, we harvested a sufficient number of colonies, and obtained a sufficient number of sequencing reads, to ensure library coverage (Methods) (36).

When this library was grown on nonselective media, all variants are well represented with similar frequencies (*SI Appendix*, Fig. S12). This result shows that 1) all 128 variants are present in the library and 2) that none of the variants are toxic to *E. coli* at the expression levels of this experiment. In contrast to the starting library, selection



 $\textbf{Fig. 3.} \quad \textbf{Gdx-Clo 7x transports quaternary ammonium compounds. (A) Representative SSM electrophysiology traces for WT-Gdx-Clo (orange) or Gdx-Clo-7x (gray) upon the properties of the pr$ $perfusion \ with \ TPA^+ \ at the \ concentrations \ indicated. For each, 2s \ of \ perfusion \ with \ activating \ solution \ are shown. Control \ experiments \ with \ protein-free \ proteoliposomes$ are shown in SIAppendix, Fig. S8A. (B) Current amplitudes as a function of TPA $^{+}$ concentration. The solid line represents a fit to the Michaelis–Menten equation with a K_m value of 6.2 mM. (C) Representative SSM electrophysiology traces for Gdx-Clo-7x upon perfusion with 5 mM Gdm⁺, methylGdm⁺, or ethylGdm⁺. Only perfusion with activating solution is shown. Control experiments with protein-free proteoliposomes are shown in SI Appendix, Fig. S8B. (D) Left, Two-step synthetic scheme for NBD-TA⁺. Reagents and conditions: (a) 4-chloro-7-nitrobenzo[c][1,2,5]oxadiazole (1 equiv), N¹,N¹-dimethylpentane-1,5-diamine (1 equiv), Et₃N (2 equiv), DMF, 90 °C, 3 h, 48 %; (b) N¹,N¹-dimethyl-N5-(7-nitrobenzo[c][1,2,5]oxadiazol-4-yl)pentane-1,5-diamine (1 equiv), Et₃N (0.1 equiv), Methyl iodide (5 equiv), DCM, rt, 1 h, 100%. *Right*, Cartoon of the transport assay using NBD-TA[±]. Proteoliposomes with internalized NBD-TA[±] (500 μM) are diluted into buffer containing 5 mM dithionite, which quenches external NBD-TA[±]. (E) Representative time courses of NBD-TA⁺ transport from liposomes containing no protein (black), WT Gdx-Clo (gray), Gdx-Clo-7x (pink), or EmrE (dark blue). Arrows show addition of dithionate (Left) and Triton (Right). Traces are normalized with respect to the fluorescence reading at 5 s, prior to dithionate addition. All traces were collected at pH 8.5, except for EmrE, which was collected at pH 7.5. (A) Time course of NBD-TA+ efflux from liposomes containing WT Gdx-Clo (pH 8.5), or Gdx-Clo-7x at the indicated pH. Traces are normalized with respect to the fluorescence reading at 5 s, prior to dithionate addition. The dark line represents the mean of three replicate time courses, and the SEM is shown by the colored regions. For clarity, only the portion of the trace after dithionate addition and before Triton addition is shown. Full traces are shown in *SI Appendix*, Fig. S10. The density of reconstituted protein in the WT Gdx-Clo and Gdx-Clo-7x samples is approximately the same, as determined by quantitative western blot (*SI Appendix*, Fig. S9). (*G*) Quantification of substrate transport shown in panel (*P*). This graph compares transport at symmetric pH 7.0 or pH 7.5 versus transport under a pH gradient (pH 7.5 internal/pH 7.0 external, shown in the Cartoon in the Upper Left side of this panel). Points show the proportion of NBD-TA⁺ quenched 540 s after dithionate addition. Lines and error bars represent the mean and SEM with significance calculated using a two-tailed *t* test.

with TPA+ or CTA+ eliminated or greatly reduced the frequency of most variants. Three independent replicates were performed for each growth condition, which showed good reproducibility with acceptable pairwise correlation coefficients above 0.71 for all comparisons, and >0.86 for most comparisons (SI Appendix, Figs. S12 and S13 and Table S4). Fig. 4 B and C shows the population-level enrichment of variants under selection versus without selection (see Eq. 1 in Methods). In this visualization, a variant with a positive score (red) will be at a population-level fitness advantage in the presence of quaternary ammonium antiseptics. A variant with a fitness score of zero (white) will be at neither a competitive advantage nor a disadvantage—it persists in the population but does not become dominant. And for variants with a negative fitness score (blue), quaternary ammonium selection decreases its proportional representation in the population. Thus, while some

variants with negative fitness scores might provide antiseptic resistance relative to WT Gdx-Clo, their representation within the variant library is still reduced under the conditions of the selection.

The variants that are enriched by the selections possess most of the originally identified seven mutations. Indeed, the most frequent variant isolated from the CTA+ screen possesses all seven, and variants lacking only A60T, A67I, or both were also enriched (Fig. 4B). For TPA⁺ resistance (Fig. 4C), variants lacking A67I, K101N, or both were enriched relative to the original library. Fig. 4D summarizes these results, which together suggest that all the cluster 1 and 2 mutations (G10I, W16G, A17T, and M39Y; see Fig. 1) are essential to confer promiscuous quaternary ammonium resistance. The cluster 3 mutations (A60T, A67I, and K101N) are, in general, less critical for this activity, but they nonetheless contribute to fitness.

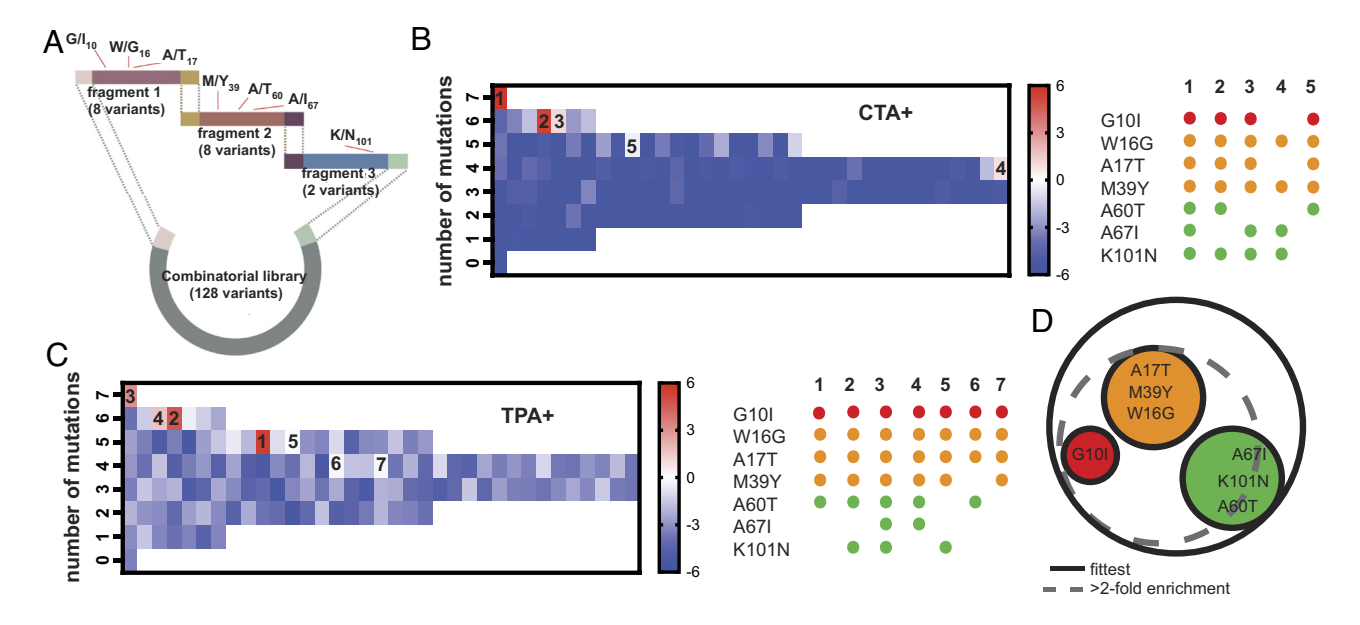


Fig. 4. Combinatorial mutagenesis to identify necessary and sufficient mutations for quaternary ammonium transport. (*A*) Schematic of the modified Gibson assembly method used to generate a combinatorial library of 128 mutational variants. (*B* and *C*) Enrichment coefficients (\log_2 scale) for library variants after selection with 120 μM CTA* (*B*) or 18 mM TPA* (*C*). The most highly represented variants are indicated (numbered in order of decreasing enrichment coefficient), with corresponding variants shown at right. Colored dots correspond to the mutational clusters from Fig. 1. Values are derived from the mean of three independent selections. Individual replicates are shown in *SI Appendix*, Fig. S12. Correlations between replicate experiments are shown in *SI Appendix*, Fig. S13 and Table S4. Enrichment coefficients for highly represented variants from the CTA* and TPA* selections are shown in *SI Appendix*, Tables S5 and S6, respectively. (*D*) Graphical summary of the selection results.

The enrichment scores for selections in CTA⁺ and TPA⁺ were correlated, but nonetheless showed appreciable variance (R² = 0.47) (*SI Appendix*, Fig. S14). We identified 11 variants that exhibited the most pronounced difference in enrichment scores between the two antiseptics (*SI Appendix*, Fig. S14 and Table S7). Variants that performed better in TPA⁺ relative to CTA⁺ tended to lack cluster 3 residues, especially A67I and K101N, suggesting the cluster 3 mutants enhance CTA⁺ transport to a greater extent than TPA⁺ transport. For variants that performed better in CTA⁺, A60T, and, notably, G10I and A17T were most frequently absent. We interpret this to mean that remodeling the immediate binding site by G10I and A17T is not as essential for CTA⁺ resistance as it is for TPA⁺ resistance, which is perhaps related to the smaller size of the CTA⁺ headgroup.

Cluster 1 and 2 Mutations Introduce the Major Functional Traits of SMR_{Oacs}. The selection experiments above report on bacterial fitness, an amalgamate measure of quaternary ammonium transport along with other factors like protein folding and membrane insertion. To dissect the contribution of the three mutational clusters to substrate binding and export specifically, we purified proteins representing each of the mutant clusters (cluster 1: G10I; cluster 2: W16G, A17T, M39Y; cluster 3: A60T, A67I, K101N), as well as additional variants with combinations of mutations suggested by our NGS analysis. All of these mutants exhibited monodisperse size exclusion profiles, indicating proper folding (SI Appendix, Fig. S15). Tryptophan fluorescence quenching experiments showed that Gdm⁺ binding was impaired by both the cluster 1 (no detectable binding) and cluster 2 (K_d ~10 mM) mutations. In contrast, the cluster 3 mutations resulted in a >10fold decrease in Gdm⁺ K_d relative to WT Gdx-Clo (Fig. 5A), perhaps due to the altered electrostatic environment conferred by K101N. For this cluster 3 mutant, we next evaluated the apparent K_d for Gdm⁺ over a range of pH values, in order to estimate the pK_a of the central glutamates. We found that the tighter Gdm+ binding of the cluster 3 mutant is accompanied by

~fivefold weaker proton binding (pK_a of 7.1, compared to a pK_a of 6.7 for WT Gdx-Clo (9); Fig. 5*B*), suggesting a substantial perturbation to the Gdm⁺/H⁺ competition necessary for antiport. Indeed, SSM electrophysiology shows that electrogenic Gdm⁺/H⁺ antiport is eliminated in the cluster 3 mutant, as in the cluster 1 and 2 mutants that fail to bind substrate (Fig. 5*C*). The cluster 2 transporter, however, retains the ability to transport ethyl- and phenylGdm⁺. This trend recapitulates the behavior of Gdx-Clo-7x and EmrE and contrasts with WT Gdx-Clo, which exhibits decreased transport currents as the hydrophobicity of the guanidinyl substrate is increased (10).

When introduced individually, none of the clusters permitted TPA⁺ binding. However, clusters 1 and 2, introduced together, were sufficient for TPA⁺ binding with a K_d of 21 mM, similar to that of Gdx-Clo-7x (Fig. 5*D*). However, we are unable to observe TPA⁺ transport by this mutant using SSM electrophysiology. We note that although this variant was relatively highly represented in our NGS, it was still ~10-fold less prevalent than Gdx-Clo-7x (*SI Appendix*, Table S4). Since TPA⁺ transport by Gdx-Clo-7x is only just above the threshold for detection by SSM electrophysiology (Fig. 3), we expect that this cluster 1 + cluster 2 mutant, and other surviving variants, might contribute to low levels of TPA⁺ transport yet not meet the lower limit for electrophysiological detection.

CTA⁺, with its small headgroup, does not require any additional mutations to support binding to WT Gdx-Clo. However, our NGS experiments show that this same complement of cluster 1 and cluster 2 mutations is essential for CTA⁺ resistance. Indeed, appreciable transport is detected for the construct with the cluster 1 and 2 mutations (labeled $4 \times$ in Fig. 5E). The introduction of additional cluster 3 mutations (Gdx-Clo- $5 \times$: A60T; Gdx-Clo- $7 \times$: A60T, A67I, K101N) further increases the rate of NBD-TA⁺ export (Fig. 5E and F). Illustrating the complex interplay between the cluster 3 mutants, transport by Gdx-Clo- $6 \times$ (A60T, K101N) is similar in rate to Gdx-Clo- $4 \times$ (P = 0.158). Although the measured difference in NBD-TA⁺ efflux from proteoliposomes reconstituted

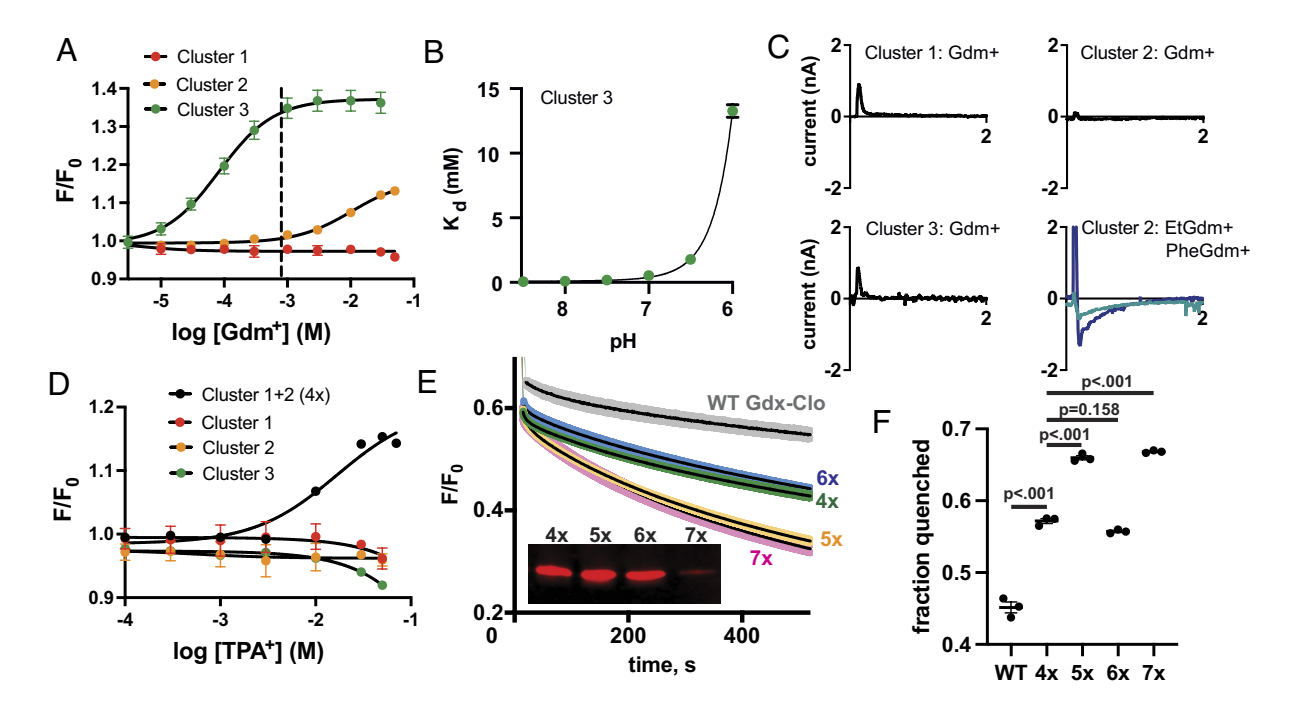


Fig. 5. Functional characterization of the three variant clusters. (A) Change in tryptophan fluorescence upon Gdm⁺ titration for cluster mutants as indicated. Datapoints represent the mean and SEM of three independent titrations. Solid lines represent fits to a single-site binding model with a K_d value of 80 µM for the cluster 3 mutant, and a K_d value of 10 mM for the cluster 2 mutant. The dashed line represents the K_d value for WT Gdx-Clo determined in Fig. 2. (B) Gdm^+ K_d values measured as a function of pH for the cluster 3 mutant. The solid line represents a fit to Eq. 3, with a K_d of 88 μ M and a composite p K_a of 7.1. Datapoints are the mean and SEM of three independent experiments. (C) SSM electrophysiology traces for indicated cluster mutants upon perfusion with the indicated substrates at concentrations of 10 mM Gdm⁺ for the cluster 1 and cluster 2 mutants; 1 mM Gdm⁺ for the cluster 3 mutant; 5 mM for EtGdm⁺ (teal) and PheGdm⁺ (dark blue). Only perfusion with activating solution is shown. (D) Change in tryptophan fluorescence upon TPA⁺ titration for cluster mutants as indicated. Datapoints represent the mean and SEM of three independent experiments. For the cluster 1 + 2 mutant, the solid line represents a fit to a single-site binding model with a K_d value of 21 mM. (E) Representative traces of NBD-TA⁺ transport by mutants 4x, 5x, 6x, and 7x. (Gdx-Clo-7x data from Fig. 3F). For clarity, only the transport phase is shown (between dithionate addition and detergent addition). All variants were reconstituted with 5 µg protein/mg lipid input. The Inset shows a western blot of the resulting proteoliposomes. The uncropped blot is shown in SI Appendix, Fig. S16. (F) Summary of three independent NBD-TA+ time courses for mutants indicated. Datapoints represent the fraction of NBD quenched 520 s. after dithionate addition, and error bars represent the SEM. Significance relative to Gdx-Clo-4x, determined using a two-tailed t test, is shown on the plot. All variants exhibit significantly more quenching than WT (P < 0.001 for all variants).

with Gdx-Clo-7x and Gdx-Clo-5x is not significant (P = 0.60), western blot analysis of proteoliposomes used for this assay showed that Gdx-Clo-7x is incorporated ~threefold less efficiently than the other Gdx-Clo variants (Fig. 5 E, Inset), suggesting that, per protein, Gdx-Clo-7x has the highest activity. Combining the results of the NGS analysis and the biochemical analysis, we conclude that cluster 1 and cluster 2 mutations are necessary and sufficient to introduce polyselective quaternary ammonium transport to the selective Gdx-Clo WT background, but that the introduction of additional mutations from cluster 3 increases the rate of quaternary ammonium export, contributing to increased fitness of the bacteria.

Discussion

The goal of this work was to identify a minimal set of mutations that converts a selective member of the SMR family, Gdx-Clo, into a promiscuous transporter of quaternary ammoniums. Because of the structural and sequence similarity between the SMR_{Oac} and $\ensuremath{\mathsf{SMR}}_{\ensuremath{\mathsf{Gdx}}}$ subtypes, we reasoned that this would be an efficient way to focus on the molecular features that are most critical for multidrug export in this family. This strategy has key advantages: First, through combinatorial mutagenesis, we were able to identify mutations that work together synergistically to confer this transport activity. Such interactions would not be revealed by single-site mutational scans (21, 37, 38). Second, this comparative approach revealed potentially important positions beyond the binding site. Although it has become clear that the entire energetic landscape

of a transporter contributes to its substrate discrimination (39–41), most mutational studies focus on the binding site as the main source of specificity (20, 37, 38). Indeed, here we found that groups of mutations peripheral to the binding site act together to encode transport polyspecificity in the SMRs. It is likely that these insights are applicable to multidrug transporters more broadly.

We identified three sensitive locations that contribute to transport of two structurally distinct quaternary ammonium compounds. The first is G10, which resides at the packing interface between helix 1 and helix 3. Based on the structures of Gdx-Clo and EmrE, we propose that the G10I mutation disrupts packing and contributes to the disorganized binding site hydrogen bond network observed in substrate-bound EmrE (18). The second mutational cluster is W16G/A17T/M39Y, located in the immediate vicinity of the central glutamate. This group of mutations removes one hydrogen bond to the central glutamate (W16G) but provides two new adjacent hydrogen bonding possibilities (A17T and M39Y). We propose that this also facilitates rotameric flexibility for the central glutamates. The third is A60T/A67I/ K101N, which is located in a region of the protein that undergoes large conformational changes during the inward-to-outward-facing conformational transition. Based on their location in the structure, and the rates observed in the CTA+ transport assay, we propose that the cluster 3 mutations improve antiseptic resistance by accelerating the rate of conformational change. None of the positions identified in this work have been previously pinpointed as playing a role in polyselectivity or substrate preference in the SMRs. Notably, however, previous mutational screens of EmrE do show that differential changes in resistance to several drugs occur for mutations at all seven positions (21, 22).

Of these seven mutations, six were subject to our focus initially because they are broadly conserved in the $\rm SMR_{Gdx}$ or $\rm SMR_{Qac}$ subtype, but differ between subtypes. Thus, it seems likely that the mutations investigated here are representative of natural mutations that contributed to the evolutionary shift in substrate specificity. Although a seventh mutation identified through directed evolution, A60T, was required to achieve robust quaternary ammonium resistance on the mutant Gdx-Clo background used in our initial screens, this mutation is not essential for quaternary ammonium transport. In follow-up resistance assays, we observed that several antiseptic-resistant variants lacked A60T, along with other cluster 3 residues.

The essential residues for polyspecific quaternary ammonium transport are contributed by cluster 1 (G10I) and cluster 2 (W16G/A17T/M39Y). By itself, G10I is nonfunctional in all scenarios that we investigated, although it overexpresses and is monodisperse upon purification. G10I does not bind or transport any guanidinium or quaternary ammonium substrate that we tested. In contrast, the cluster 2 mutations are less severe when introduced on the WT Gdx-Clo background. Although this complement of mutations decreases the protein's affinity for Gdm † by >10-fold, the cluster 2 mutant is capable of transporting substituted guanidinium ions with the same substrate hydrophobicity trend seen for EmrE (10). More importantly, the cluster 2 mutations permit introduction of the otherwise-intolerable G10I.

The combination of G10I and the cluster 2 mutations meets our study's minimal requirements for promiscuous quaternary ammonium transport. Together, the four mutations enable binding of the bulky TPA⁺, TPA⁺ resistance, and CTA⁺ resistance and transport. We hypothesize that these mutations contribute to binding pocket flexibility, which not only permits TPA+ binding, but also allows CTA⁺ to penetrate more deeply into the aqueous vestibule. Whereas CTA+ hovers just above the central glutamates in the WT-like structure determined here, all transported substrates for both EmrE and Gdx-Clo reside in the plane of the central glutamates (9, 10, 18). At this position, a substrate is able to disrupt the interaction between the glutamate and the tyrosine switch (Y59 in Gdx-Clo/Y60 in EmrE), which has been proposed to trigger the conformational change essential for transport (18, 42). Thus, despite their differences in bulk, we propose that transport of TPA+ and CTA+ both originate in the loosening of the hydrogen bond network in the binding site, which allows sidechains to rearrange so that hydrophobic or bulky substrates can access the depths of the binding pocket. In the Gdx-Clo-7x mutant, the gain of quaternary ammonium transport activity is accompanied by other traits characteristic of EmrE and other SMR_{Qacs}, including the loss of Gdm⁺ transport activity and preference for additional substrate hydrophobicity (8).

Our experiments also suggest a plausible evolutionary pathway between the selective SMR_{Gdx} subtype and the polyspecific $SMR_{Qac}s$. In the evolution of quaternary ammonium transport by SMR proteins, it is unlikely G10I could have arisen early, as it abolishes transport function. And while the cluster 2 mutations do not eliminate transport of compounds like phenyl Gdm^{+} , the protein loses its ability to transport the native metabolite Gdm^{+} without gaining a new physiologically relevant transport function. This implies that the early introduction of cluster 2 mutations is also not a viable evolutionary trajectory (although it is possible that an unknown natural substrate acted as a bridge). Indeed, protein evolution often requires accumulation of functionally neutral mutations that are permissive for later mutations that change the

function (43). It is possible that the cluster 3 mutations contributed to this—by increasing binding affinity to Gdm^+ , they may have offset the deleterious effect of cluster 2 mutations that, on their own, weaken Gdm^+ binding. It is also possible that other permissive mutations arose during the evolution of an ancestral SMR, and that these are not recapitulated by our mutation of extant SMR_{Gdx} Gdx-Clo. Future studies will be required to test these possibilities.

In summary, we have established a set of necessary and sufficient residues that facilitate quaternary ammonium transport by SMR transporters (44). These residues are conserved among polyspecific SMR_{Qacs} and thus are likely to represent naturally important positions in model transporters like EmrE. Notably, these mutations are peripheral to the binding pocket, and the changes to specificity are not the result of mutations to residues that interact directly with the substrate. By zeroing in on a minimal set of mutations, we provide insight into the essential molecular determinants of polyspecific transport, with implications for other promiscuous drug exporters.

Methods

Quaternary Ammonium Resistance Assays. Overnight cultures (12 to 16 h) of Δ emrE E. coli (Keio collection, Coli Genetic Stock Center, New Haven, CT) bearing the SMR genes in the pBAD24 vector were diluted to OD_{600} of 0.05 with LB media containing 13.3 mM arabinose to induce protein expression, 50 µg/mL kanamycin, and 100 µg/mL carbenicillin and then grown to OD_{600} 0.5 to 0.8 (37 °C, 240 rpm). 10-fold serial dilutions were spotted onto plates containing 70 mM K₂HPO₄, pH 7.2, 0.2% arabinose, antibiotic, and 120 µM cetrimonium bromide or 18 mM tetrapropylammonium chloride, and examined for growth after 24 to 48 h. Parallel control plates without quaternary ammonium compound were prepared for each experiment.

Directed Evolution. Directed evolution was performed on a background construct of Gdx-Clo with G10I, W16G, A17T, M39Y, A67I, and K101N mutations in pBAD24 using the GeneMorph II EZClone Domain Mutagenesis Kit (Stratagene) with the manufacturer's protocol and the following primers:

Forward Primer: 5'-CAGGAGGAATTCACCATGGCGTGGCTGATC-3' Reverse Primer: 5- ACAGCCAAGCTTATTAGCTGCTGGTCGCTTT-3'

The library was transformed into high-efficiency, electrocompetent DH5 α cells, and the transformants were collected to prepare a stock of the library plasmid DNA. For screening, the purified library was transformed into the $\Delta emrE$ E. coli strain via electroporation and used to inoculate an overnight growth. The overnight culture was diluted to OD_600 of 0.05, and plasmid expression was induced with 0.2% arabinose. The culture was grown until the OD_600 reached 0.5, and serial dilutions were plated on buffered LB with arabinose and 200 μ M-300 μ M CTA $^+$. After 24 h of growth, plasmid DNA was isolated from individual colonies and sequenced. Variants that emerged from the CTA $^+$ selection were subjected to a further round of selection in the presence of 20 mM to 30 mM TPA $^+$.

Combinatorial Library Construction, Selection Assays, and Illumina **Sequencing.** Gene blocks (*SI Appendix*, Table S8) were synthesized by Azenta and prepared as a pooled master mix (10 $ng/\mu L$ for each fragment). Fragments were assembled into the pBAD24 vector using HiFi DNA Assembly Kit (New England Biolabs) with 1-h, 50 °C incubation and 0.2 pmol total fragments. After transformation, half of the recovery culture was plated on LB agar with carbenicillin to evaluate transformation efficiency, and the remaining half used to inoculate an overnight culture (LB with carbenicillin) for purification of the combinatorial plasmid library. The assembled combinatorial library was transformed into $\Delta emrE$ E. coli via electroporation, prepared for resistance assays as described above, and plated as 10-fold serial dilutions on LB with 120 μ M cetrimonium bromide, 20 mM TPA⁺, or neither, without additional antibiotics. Plates with >1,000 isolated colonies were resuspended, and the population plasmid DNA was isolated. This number of colonies corresponds to a >95% chance that there is a clone present for each of the 128 variants in the input library (36). Illumina adapters were added via PCR using the following primers:

Forward Illumina Adapter: 5'-ACACTCTTTCCCTACACGACGCTCTTCCGATCTXXXX-3' Reverse Illumina Adapter: 5'-GACTGGAGTTCAGACGTGTGCTCTTCCGATCTXXXX-3' Next-generation (Illumina) sequencing was performed by Azenta (Amplicon-EZ). For each experiment, >135,000 quality reads were obtained, corresponding to >1,000-fold coverage of each variant in the unselected population, which is sufficient for a selection of this kind (45). Processing included removal of reads < 10. Three independent library preparations and selections were performed for each experiment. The enrichment coefficients for variant i, ε_i , is given by

$$\varepsilon_i = \log_2\left(\frac{f_{\text{sele}}}{f_{\text{control}}}\right), \quad [\mathbf{1}]$$

where f_{sele} and f_{control} are given by the mean number of reads for the mutant (N_i) mean of three experimental replicates), divided by the mean number of total reads (N_{tot}) for the library,

$$f = \frac{N_l}{N_{\text{tot}}},$$
 [2]

for libraries plated with and without quaternary ammonium compound, respectively.

Protein Purification and Liposome Reconstitution. Proteins were expressed and purified as previously described (8, 10). Briefly, hexahistidine-tagged proteins were overexpressed in E. coli (C43-DE3), extracted from E. coli membranes with 3% n-decyl-β-D-maltoside (DM; Anatrace), and purified using cobalt affinity resin and size exclusion chromatography. Purified protein was reconstituted into proteoliposomes (E. coli polar lipid extract, Avanti Polar Lipids, Alabaster, AL) by dialysis in 100 mM KCl, 100 mM K₂HPO₄, pH 7.52 as described (8, 10). For the NBD-TA+ transport assay, proteoliposomes were prepared with a protein:lipid ratio of 0.5 to 5 $\mu g/mg$. For SSM electrophysiology experiments, proteoliposomes were prepared with a protein: lipid ratio of 40 $\mu g/mg$. Proteoliposomes were stored at -80 °C until use.

Synthesis of NBD-TA⁺. All commercial reagents and solvents were used as supplied without further purification. Proton nuclear (1H) NMR spectroscopy was performed on a Bruker Advance 400 NMR spectrometer. ¹H NMR shifts are reported in parts per million (ppm) and are referenced to tetramethylsilane (0.00 ppm) or residual DMSO (2.50 ppm). In the spectral data reported (SI Appendix, Fig. S17), the format (δ) chemical shift (multiplicity, J values in Hz, integration) was used with the following abbreviations: s = singlet, d = doublet, t = triplet, q = quartet, p = pentet, m = multiplet. Electrospray ionization (ESI) mass spectral (MS) analysis was performed on a Thermo Scientific LCQ Fleet mass spectrometer. The final products were purified by reverse-phase HPLC (RP-HPLC) with solvent A (0.1% of TFA in water) and solvent B (0.1% of TFA in CH₃CN) as eluents with a flow rate of 45 mL/min. All final compounds have purity ≥95% as determined by Waters ACQUITY ultraperformance liquid chromatograph (UPLC) using reverse phase column (SunFire, C18, 5 μ m, 4.6 \times 150 mm²) and a gradient of solvent A (H₂O with 0.1% of TFA) and solvent B (CH₃CN with 0.1% of TFA) (SI Appendix, Fig. S18). N^1 , N^1 -dimethylpentane-1,5-diamine (1). A solution of NBD-Cl (100 mg, 0.5 mmol, 1 equiv.) in 0.5 mL anhydrous DMF was added dropwise in 5 min under a nitrogen atmosphere at room temperature, to a stirred solution of (5-aminopentyl) dimethylamine dihydrochloride (0.5 mmol, 1 equiv.) and triethylamine (154 µL, 1 mmol, 2 equiv) in 1 mL of anhydrous DMF. The reaction was stirred for 3 h at 90 °C. The reaction was cooled to ambient temperature and then subsequently purified by preparative reverse-phase HPLC by direct injection of the reaction mixture using a gradient of 10%_50% B in 40 min_60mL. The product eluted at 26% B. Fractions were combined and lyophilized to produce compound 1 as the iminium (70 mg, 0.25 mmol) as a mahogany-colored solid in 48% yield. ¹H NMR (400 MHz, DMSO- d_6) δ 10.30 (s, 1H), 9.55 (s, 1H), 8.51 (d, J = 9.0 Hz, 1H), 6.44 (d, J = 9.0 Hz, 1H), 3.49 (d, J = 7.6 Hz, 2H), 3.03 - 2.96(m, 2H), 2.72 (s, 3H), 2.71 (s, 3H), 1.76 - 1.64 (m, 4H), 1.39 (p, J = 7.7 Hz, 2H).ESI-MS m/z $(M + H)^+ = 294.16$.

N,N,N-trimethyl-5-((7-nitrobenzo[c][1, 2, 5]oxadiazol-4-yl)amino)pentan-1aminium (2). Triethylamine (2.3 µL, 0.02 mmol) was added to a stirred solution of compound 1 (50 mg, 0.17 mmol) in 3 mL of DCM. Methyl iodide (53 µL, 0.85 mmol, 5 equiv.) was then added, and the reaction mixture turned a reddish-brown color.

The reaction was stirred for 1 h at ambient temperature. The reaction mixture was purified by preparative reverse-phase HPLC by direct injection of the reaction mixture using the gradient of 10%_50% B in 40 min_60 mL. The product eluted at 25% B. Fractions were combined and lyophilized to produce compound 2 (52 mg, 0.17 mmol) as a mahogany-colored semisolid in 100% yield. ¹H NMR (400 MHz, DMSO- d_6) δ 9.54 (s, 1H), 8.53 (d, J = 9.0 Hz, 1H), 6.44 (d, J = 9.0 Hz, 1H), 3.51 (overlapping, 2H), 3.28 - 3.23 (m, 2H), 3.03 (s, 9H), 1.78 - 1.68 (m, 4H), 1.38 (q, J = 7.7 Hz, 2H). ESI-MS m/z $(M + H)^+ = 308.24$.

NBD-TA⁺ Transport. Proteoliposomes were preloaded with 500 μM NBD-TA⁺, subjected to 5 freeze/thaw cycles, and extruded 25 times through a 400-nm membrane filter. Liposomes were diluted 200-fold in assay buffer [100 mM KCl, 100 mM K₂HPO₄ 10 mM 4-(2-Hydroxyethyl)-1-piperazinepropanesulfonate (EPPS), pH 7.0 to 8.8]. Freshly prepared sodium hydrosulfite (dithionate) was added to a final concentration of 5 mM to guench external NBD-TA⁺. For experiments carried out at symmetric pH, valinomycin (2 µg/mL) and carbonyl cyanide-ptrifluoromethoxyphenylhydrazone (FCCP; 1 $\mu g/mL$) were added to prevent buildup of an electrochemical gradient. NBD-TA $^+$ fluorescence was monitored (λ_{ex} = 470 nm, λ_{em} = 540 nm) using a fluorimeter (FP-8300, Jasco, Easton, MD) for 540 s prior to addition of 0.1% Triton X-100 to solubilize liposomes. Experiments were done in triplicate for each of two independent biochemical purifications.

Tryptophan Fluorescence Binding Assay. Assay buffer was matched to the size exclusion chromatography buffer [100 mM NaCl, 10 mM 4-(2-Hydroxyethyl) piperazine-1-ethanesulfonate (HEPES), pH 8.0, 4 mM DM]. Changes in tryptophan fluorescence upon substrate addition were monitored using a Jasco FP8300 fluorimeter ($\lambda_{ex} = 280$ nm, $\lambda_{em} = 300$ to 400 nm) and fit to a single-site binding isotherm. The \overline{pH} dependence of the apparent K_d was fit to the following equation, which assumes equal pKa values for the two binding site glutamates, to determine the pK_a and K_d:

$$K_{d,app} = (K_d) * \left(1 + \left(\frac{[H^+]}{K_a}\right)\right)^2.$$
 [3]

SSM Electrophysiology. SSM electrophysiology measurements were performed using the SURFE²R N1 (Nanion Technologies). Sensor preparation and verification of the sensor capacitance and conductance was performed exactly as described previously (10). Experiments typically involved a series of three perfusions: a 2 s. perfusion with buffer, a 2 s. perfusion with activating solution (buffer plus substrate at the concentration indicated in the text), and a 4 s. perfusion with buffer to wash away substrate. For a single sensor, currents from three perfusions with activating solution were averaged; these currents did not vary by more than 10%. Sensors were prepared from at least two independent protein purifications.

Protein Crystallization and X-ray Crystallography. Purification of L10 monobodies and Gdx-Clo A60T was performed as previously described (10). Freshly purified L10 and Gdx-Clo (10 mg/mL each) were mixed (2 monobody:1 transporter molar ratio) and combined with 50 µM CTA⁺ bromide prior to mixture with crystallization solution. Crystals formed at 22 °C in 100 mM CaCl₂, 100 mM N-(2-acetamido)iminodiacetic acid (ADA) pH 6.75, and 33% PEG 600 and were frozen in liquid nitrogen prior to data collection at 13.5 keV at the Life Sciences Collaborative Access Team beamline 21-ID-D at the Advanced Photon Source, Argonne National Laboratory. Processed data were subjected to anisotropic truncation using Staraniso (46), and phases were calculated by molecular replacement with Phaser (47), with iterative rounds of refinement in Phenix (48) and model building in Coot (49). Polder omit maps were prepared using Phenix (50).

Data, Materials, and Software Availability. Atomic coordinates for the crystal structure has been deposited in the Protein Data Bank under accession number 8VXU (51). Raw sequencing data have been deposited in the NCBI Sequencing Read Archive with BioProject ID PRJNA1104635 (52). Processed sequencing data (reads) are available as Dataset S1. All other data are included in the manuscript and/or supporting information.

ACKNOWLEDGMENTS. This work was supported by NSF CAREER award 1845012 to R.B.S. This research used resources of the Advanced Photon Source, a U.S.

Department of Energy (DOE) Office of Science User Facility operated for the DOE Office of Science by Argonne National Laboratory under Contract No. DE-ACO2-06CH11357. Use of the LS-CAT Sector 21 was supported by the Michigan

Economic Development Corporation and the Michigan Technology Tri-Corridor (Grant 085P1000817). This paper was developed from portions of O.E.B.'s Ph.D. dissertation.

- A. Oberai, Y. Ihm, S. Kim, J. U. Bowie, A limited universe of membrane protein families and folds. Protein Sci. 15, 1723-1734 (2006).
- A. A. Aleksandrova, E. Sarti, L. R. Forrest, MemSTATS: A benchmark set of membrane protein symmetries and pseudosymmetries. J. Mol. Biol. 432, 597-604 (2020).
- S. J. Fleishman et al., Quasi-symmetry in the cryo-EM structure of EmrE provides the key to modeling its transmembrane domain. J. Mol. Biol. 364, 54-67 (2006).
- E. A. Morrison et al., Antiparallel EmrE exports drugs by exchanging between asymmetric structures Nature 481, 45-50 (2012).
- L. R. Forrest, Structural symmetry in membrane proteins. Annu. Rev. Biophys. 44, 311-337 (2015).
- S. Schuldiner, EmrE, a model for studying evolution and mechanism of ion-coupled transporters. Biochim. Biophys. Acta 1794, 748-762 (2009).
- O. E. Burata, T. J. Yeh, C. B. Macdonald, R. B. Stockbridge, Still rocking in the structural era: A molecular overview of the small multidrug resistance (SMR) transporter family. J. Biol. Chem. 298, 102482 (2022).
- A. A. Kermani, C. B. Macdonald, R. Gundepudi, R. B. Stockbridge, Guanidinium export is the primal function of SMR family transporters. *Proc. Natl. Acad. Sci. U.S.A.* **115**, 3060-3065 (2018).
- R. M. Lucero, K. Demirer, T. J. Yeh, R. B. Stockbridge, Transport of metformin metabolites by quanidinium exporters of the small multidrug resistance family. J. General Physiol. 156, e202313464 (2024)
- A. A. Kermani et al., The structural basis of promiscuity in small multidrug resistance transporters. Nat. Commun. 11, 6064 (2020).
- H. Yerushalmi, M. Lebendiker, S. Schuldiner, EmrE, an Escherichia coli 12-kDa multidrug transporter, exchanges toxic cations and H+ and is soluble in organic solvents. J. Biol. Chem. 270, 6856-6863
- 12. D. Rotem, S. Schuldiner, EmrE, a multidrug transporter from Escherichia coli, transports monovalent and divalent substrates with the same stoichiometry. J. Biol. Chem. 279, 48787-48793 (2004).
- D. C. Bay, K. L. Rommens, R. J. Turner, Small multidrug resistance proteins: A multidrug transporter family that continues to grow. Biochim. Biophys. Acta 1778, 1814-1838 (2008).
- M. Gillings et al., The evolution of class 1 integrons and the rise of antibiotic resistance. J. Bacteriol. **190**, 5095-5100 (2008).
- Y. G. Zhu et al., Continental-scale pollution of estuaries with antibiotic resistance genes. Nat. Microbiol. 2, 16270 (2017).
- S. Domingues, G. J. da Silva, K. M. Nielsen, Global dissemination patterns of common gene cassette arrays in class 1 integrons. Microbiology (Reading) 161, 1313-1337 (2015).
- W. H. Gaze, N. Abdouslam, P. M. Hawkey, E. M. Wellington, Incidence of class 1 integrons in a quaternary ammonium compound-polluted environment. Antimicrob. Agents Chemother. 49, 1802-1807 (2005).
- A. A. Kermani et al., Crystal structures of bacterial small multidrug resistance transporter EmrE in complex with structurally diverse substrates. Elife 11, e76766 (2022).
- T. R. Muth, S. Schuldiner, A membrane-embedded glutamate is required for ligand binding to the multidrug transporter EmrE. EMBO J. 19, 234-240 (2000).
- S. Brill, O. Sade-Falk, Y. Elbaz-Alon, S. Schuldiner, Specificity determinants in small multidrug transporters. J. Mol. Biol. 427, 468-477 (2015).
- C. Wu et al., Identification of an alternating-access dynamics mutant of EmrE with impaired transport. J. Mol. Biol. 431, 2777-2789 (2019).
- M. Saleh, D. C. Bay, R. J. Turner, Few conserved amino acids in the small multidrug resistance transporter EmrE influence drug polyselectivity. Antimicrob. Agents Chemother. 62, e00461-18 (2018).
- E. A. Morrison, K. A. Henzler-Wildman, Transported substrate determines exchange rate in the multidrug resistance transporter EmrE. *J. Biol. Chem.* **289**, 6825–6836 (2014).
 A. E. Robinson, N. E. Thomas, E. A. Morrison, B. M. Balthazor, K. A. Henzler-Wildman,
- New free-exchange model of EmrE transport. Proc. Natl. Acad. Sci. U.S.A. 114, E10083-E10091 (2017)
- R. Dastvan, A. W. Fischer, S. Mishra, J. Meiler, H. S. McHaourab, Protonation-dependent conformational dynamics of the multidrug transporter EmrE. Proc. Natl. Acad. Sci. U.S.A. 113, 1220-1225 (2016).

- 26. M. K. Cho, A. Gayen, J. R. Banigan, M. Leninger, N. J. Traaseth, Intrinsic conformational plasticity of native EmrE provides a pathway for multidrug resistance. J. Am. Chem. Soc. 136, 8072-8080 (2014).
- $J.\ Li, A.\ Sae\ Her, N.\ J.\ Traaseth, Asymmetric\ protonation\ of\ glutamate\ residues\ drives\ a\ preferred$ transport pathway in EmrE. Proc. Natl. Acad. Sci. U.S.A. 118, e2110790118 (2021).
- J. W. Nelson, R. M. Atilho, M. E. Sherlock, R. B. Stockbridge, R. R. Breaker, Metabolism of free guanidine in bacteria is regulated by a widespread riboswitch class. Mol. Cell 65, 220-230 (2017).
- C. W. Sikora, R. J. Turner, SMR proteins SugE and EmrE bind ligand with similar affinity and stoichiometry. Biochem. Biophys. Res. Commun. 335, 105-111 (2005).
- B. Ploier, A. K. Menon, A fluorescence-based assay of phospholipid scramblase activity. J. Vis. Exp 115, 54635 (2016), 10.3791/54635.
- E. Lambert, A. R. Mehdipour, A. Schmidt, G. Hummer, C. Perez, Evidence for a trap-and-flip mechanism in a proton-dependent lipid transporter. Nat. Commun. 13, 1022 (2022).
- I. Menon *et al.*, Opsin is a phospholipid flippase. *Curr. Biol.* **21**, 149–153 (2011). V. Kalienkova, V. Clerico Mosina, C. Paulino, The Groovy TMEM16 family: Molecular mechanisms of lipid scrambling and ion conduction. *J. Mol. Biol.* **433**, 166941 (2021).
- H. Yerushalmi, S. Schuldiner, An essential glutamyl residue in EmrE, a multidrug antiporter from *Escherichia coli. J. Biol. Chem.* **275**, 5264–5269 (2000).
- R. B. Stockbridge, The application of Poisson distribution statistics in ion channel reconstitution to determine oligomeric architecture. Methods Enzymol. 652, 321-340 (2021).
- W. M. Patrick, A. E. Firth, J. M. Blackburn, User-friendly algorithms for estimating completeness and diversity in randomized protein-encoding libraries. Protein Eng. 16, 451-457 (2003).
- G. Meier et al., Deep mutational scan of a drug efflux pump reveals its structure-function landscape. Nat. Chem. Biol. 19, 440-450 (2023).
- P. Saini et al., Alanine scanning of transmembrane helix 11 of Cdr1p ABC antifungal efflux pump of Candida albicans: Identification of amino acid residues critical for drug efflux. J. Antimicrob. Chemother. 56, 77-86 (2005).
- F. Marinelli, J. D. Faraldo-Gomez, Conformational free-energy landscapes of a Na+/Ca2+ exchanger explain its alternating-access mechanism and functional specificity. Proc. Natl. Acad. Sci. U.S.A. 121, e2318009121 (2024).
- D. Mitrovic et al., Reconstructing the transport cycle in the sugar porter superfamily using
- coevolution-powered machine learning. Elife 12, e84805 (2023).
 P. J. Spreacker et al., Activating alternative transport modes in a multidrug resistance efflux pump to confer chemical susceptibility. Nat. Commun. 13, 7655 (2022).
- J. V. Vermaas, S. B. Rempe, E. Tajkhorshid, Electrostatic lock in the transport cycle of the multidrug resistance transporter EmrE. Proc. Natl. Acad. Sci. U.S.A. 115, E7502-E7511 (2018).
- T. N. Starr, J. W. Thornton, Epistasis in protein evolution. Protein Sci. 25, 1204-1218 (2016).
- O. E. Burata, "The basis of substrate promiscuity in membrane protein drug transporters using the small multidrug resistance (SMR) family as simple models," Ph.D. Thesis, University of Michigan, Ann Arbor, MI (2023)
- C. A. Kowalsky et al., High-resolution sequence-function mapping of full-length proteins. PLoS One 10, e0118193 (2015).
- I. J. Tickle et al., STARANISO (Global Phasing Ltd., Cambridge, United Kingdom, 2018)
- A. J. McCoy et al., Phaser crystallographic software. J. Appl. Crystallogr. 40, 658-674 (2007).
- D. Liebschner et al., Macromolecular structure determination using X-rays, neutrons and electrons: Recent developments in Phenix. Acta Crystallogr. D Struct. Biol. 75, 861-877 (2019).
- P. Emsley, B. Lohkamp, W. G. Scott, K. Cowtan, Features and development of Coot. Acta Crystallogn. D Biol. Crystallogr. 66, 486-501 (2010).
- D. Liebschner et al., Polder maps: Improving OMIT maps by excluding bulk solvent. Acta Crystallogn. D Struct. Biol. 73, 148-157 (2017).
- $O.\ E.\ Burata,\ R.\ B.\ Stockbridge,\ Crystal\ structure\ of\ Gdx-Clo\ A60T\ from\ Small\ Multidrug\ Resistance$ family of transporters in complex with cetyltrimetylammonium. Protein Data Bank. https://www. rcsb.org/structure/8VXU. Deposited 6 February 2024.
- O. E. Burata, R. B. Stockbridge, Gdx-Clo 7X Combinatorial Library Screening in Quaternary Ammonium Compounds. NCBI Sequencing Read Archive. https://www.ncbi.nlm.nih.gov/bioproject/ PRJNA1104635. Deposited 25 April 2024.